

Collective cluster nucleation dynamics in 2D Ising quantum magnets

Philip Osterholz,¹ Fabio Bensch,¹ Shuanghong Tang,¹ Silpa Baburaj Sheela,¹ Igor Lesanovsky,² and Christian Groß^{3,*}

¹*Physikalisches Institut, Eberhard Karls Universität Tübingen, 72076 Tübingen, Germany*

²*Institut für Theoretische Physik and Center for Integrated Quantum Science and Technology, Universität Tübingen, Auf der Morgenstelle 14, 72076 Tübingen, Germany*

³*Physikalisches Institut and Center for Integrated Quantum Science and Technology, Eberhard Karls Universität Tübingen, 72076 Tübingen, Germany*

(Dated: December 5, 2025)

Strongly interacting many-body systems often show collective properties that are non-trivially related to the microscopic degrees of freedom. Collectivity is responsible for intriguing ground state properties, for example, in superconductors. However, collective effects may also govern the non-equilibrium response of quantum systems, not only in condensed matter physics but also in quantum field theories modeling the properties of our universe. Understanding emergent collective dynamics from first principles, in particular in non-perturbative regimes, is therefore one of the central challenges in quantum many-body physics. Here we report on the observation of collective cluster nucleation in 2D quantum Ising systems realized in an atomic Rydberg array. We observe a confined regime in which the steady-state cluster size is energy-dependent and a deconfined regime characterized by kinetically constrained dynamics of cluster nucleation. Our results mark a qualitative leap for quantum simulations with Rydberg arrays and shed light on highly collective non-equilibrium processes in one of the most important textbook models of condensed matter physics with relevance from quantum magnets and the kinetics of glass formers to cosmology.

Correlated dynamics underlies many collective phenomena, including metastability and false vacuum decay [1–3], bubble nucleation and confinement [4–7], and kinetically constrained dynamics with the subsequent slow thermalization due to Hilbert space fragmentation [8–10]. The quantum Ising model in transverse and longitudinal fields serves as a minimal model system to explore many aspects of such non-equilibrium physics. Of central importance is the interplay between interactions, single-particle energy shifts in external fields, and quantum or thermal fluctuations. Experimentally, the Ising model is realized in atomic, ionic, or solid-state-based quantum simulators, and several features of its dynamics have already been explored. In one-dimensional lattice systems, metastable behavior and confinement of domain walls have been observed, which are caused by a size-dependent energy of the domain [11–14]. Closely related to this is the phenomenology of false vacuum decay, that is, the collective transition from one ordered quantum state to another. This physics has been probed in the continuum with Bose-Einstein condensates in an effectively one-dimensional setting [15]. In higher dimensions, the physics becomes even richer. With neutral atom arrays, string-breaking, a prominent example of confinement in gauge theories, has been observed [16]. Avalanche dynamics has been probed in atomic systems with competing short- and long-range interactions in optical cavities [17] and lattices [18]. In higher-dimensional lattices, kinetically constrained magnetic dynamics emerge where the spatial shape of collective spin clusters becomes important [7, 9, 10, 19]. At the so-called deconfinement point, the energy needed to grow an existing cluster by flipping an adjacent spin is matched by the energy gain in the external field. There, avalanche-

like domain growth with strong geometric constraints is predicted [8].

In our experiments, we study collective cluster formation in two-dimensional Ising systems, realized in atomic arrays with strong van der Waals interactions between Rydberg atoms. While the majority of experiments on this platform use the Rydberg blockade [20] for implementing many-body spin models, we utilize an anti-blockade, where Rydberg atoms facilitate the excitation of nearby atoms [21]. In this setting, strong spin-motion coupling demands exquisite control over the atomic positions to implement unitary dynamics within the many-atom pseudo spin-1/2 subspace formed by the atomic ground and one Rydberg state [22–24]. Indeed, coherent dynamics has recently been demonstrated, and quantum many-body scars and kinetically constrained dynamics in one-dimensional arrays have been studied [25, 26]. Earlier experiments explored Rydberg facilitation in continuum systems, where dissipation played a major role [27–31]. Our system is initially at zero temperature in the pseudo-spin sector, and dissipation has little effect on the fast timescales on which we study the collective dynamics. With the experiments reported here, we demonstrate that facilitated Rydberg dynamics can be coherently controlled in large two-dimensional arrays. This paves the way to study a wide range of new phenomena on these versatile quantum simulators, including exotic equilibrium quantum states [32], dynamics of collective spin-clusters [33], thermalization in strongly constrained systems [8, 9], and equilibration in glassy systems [34].

Our experiments are based on potassium-39 atoms in optical tweezer arrays [35]. We start with the preparation of a 2D square array of 15×15 tweezers with a nearest-neighbor distance of $7 \mu\text{m}$, and load a single atom in each

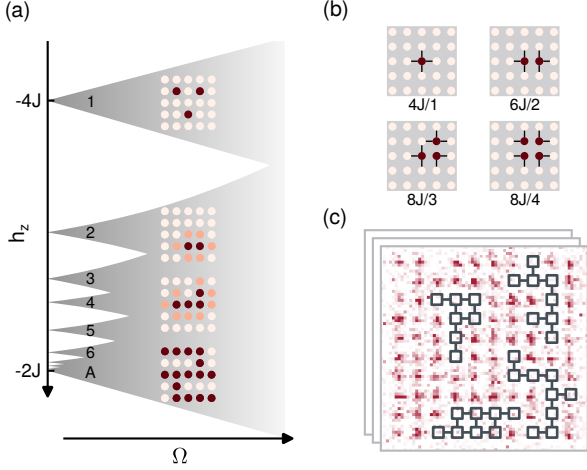


FIG. 1. **Illustration of the many-body spectrum in a 2D Ising model.** (a) Sketch of the quench response of the square-lattice Ising model with nearest-neighbor interactions for an initial state with all spins in the $|\downarrow\rangle$ -state (light red circles) as a function of h_z and Ω . For quenches to weak transverse field Ω , the response is sharp and concentrated around discrete many-body resonances in h_z . At $h_z = h_z^S = -4J$, single spin flips are resonant, while confined clusters of increasing size (dark red circles with cluster sizes indicated by the numbers) become resonant at larger h_z up to the deconfinement point at $h_z = h_z^A = -2J$ (marked with the letter A). Here, the dynamics are characterized by avalanche-like growth of clusters. With increasing Ω , the resonances broaden (indicated by the gray shading), shift, and the cluster sizes mix due to quantum fluctuations (light red circles). (b) Confined clusters behave as collective objects with characteristic shapes determined by energetic constraints. In the classical ($\Omega \rightarrow 0$) limit, the excitation energy of a cluster is determined by the number of unsatisfied bonds (black lines) along its perimeter, each increasing the energy by J . The collective resonance is located at the total cluster energy divided by the number of spins in the cluster, as indicated below the cluster sketches. The square-shaped cluster at the lower right is located at an energy of $h_z = -2J$, where the addition of further spins is resonant such that the cluster size is unconfined. (c) Typical experimental snapshot after a quench to the deconfinement resonance at $h_z = -2J$. Four clusters of Rydberg atoms, that is, connected sites of flipped spins identified by missing atoms, are highlighted by the linked black squares.

tweezer with about 65 % probability. This loading is done from a reservoir light sheet and under continuous gray molasses cooling [36]. We then arrange the atoms into a central 10×10 array of $N = 100$ and assure its isolation by clearing atoms from the tweezers surrounding the array. In a single sorting step, we reach an occupation of 92 % in the target region. The tweezer array is carefully position corrected and homogenized to sub-percent peak-to-peak intensity deviations [37], a critical step for high-fidelity imaging in our tweezers formed by 1064 nm light and for Raman sideband cooling. The latter we perform in three dimensions and reach an in-plane ground-state

population of 90 % and in all directions of 70 %. This is critical to mitigate position-fluctuation-induced disorder. The final step to prepare the initial state is to optically pump the atoms to the $4S_{1/2} |F = 2, m_F = 2\rangle \equiv |\downarrow\rangle$ hyperfine state.

We induce strong interactions between the atoms by exciting them to the $75S |J = 1/2, m_J = 1/2\rangle \equiv |\uparrow\rangle$ Rydberg state using a two-photon transition via the intermediate $5P_{3/2} |F = 3/2, m_F = 3/2\rangle$ state. We reach maximal Rabi frequencies Ω of $\Omega_{\max} \approx 2\pi \times 2$ MHz across the entire central array. At $7\mu\text{m}$ distance the interactions amount to an energy shift of $U_0/\hbar = 2\pi \times 11$ MHz with \hbar being the reduced Planck constant. Repulsive forces between Rydberg atoms limit the observation time and restrict the maximal controllable interaction strength [36]. The resulting antiferromagnetic Ising Hamiltonian is

$$\begin{aligned} \hat{H}/\hbar &= \sum_{i \neq j} \frac{U_{ij}}{2} \hat{R}_i \hat{R}_j - \Delta \sum_i \hat{Z}_i - \Omega \sum_i \hat{X}_i \\ &\approx J \sum_{\langle i, j \rangle} \hat{Z}_i \hat{Z}_j - h_z \sum_i \hat{Z}_i - \Omega \sum_i \hat{X}_i, \end{aligned}$$

which we have written in standard Ising form in terms of the spin-1/2 operators \hat{X}_i , \hat{Z}_i at site i by using the relation $\hat{R}_i = \hat{Z}_i + \hat{\mathbb{I}}_i/2$ with the local projector to the Rydberg state \hat{R}_i and the identity operator $\hat{\mathbb{I}}_i$. The interaction strength between nearest neighbors is $J = U_0/2$. The laser detuning Δ enters as an effective longitudinal field $h_z = (\Delta + \frac{N U_0}{2})$, and the number of nearest neighbors is $N = 4$ in our geometry. In rewriting the Hamiltonian, we discard longer-range interactions, which are weaker than the diagonal one with $U_0/8 < \Omega_{\max}$. While these increase the cluster energies quantitatively, they do not change the qualitative physics. We will comment on their effect where appropriate. Also, effective local longitudinal fields on the edge of the system and around missing atoms are not important here.

In the classical limit $\Omega = 0$ and for $h_z = 0$, the fully polarized states are degenerate and the highest energy states of the Hamiltonian. The number of unsatisfied bonds (bonds with opposite spins) determines the energy difference of other states to the two extremal states. In a closed quantum system, the high-energy spectrum of our antiferromagnetic case maps to the low-energy spectrum of the ferromagnetic Ising model, in which cluster formation and metastability are usually discussed [2, 4, 38]. A finite longitudinal field h_z biases one of the spin orientations against the other, such that the domain wall energy cost can be compensated. For the system being initially in the $|\downarrow\rangle^{\otimes N}$ state, this leads to a characteristic spectrum of resonances in h_z , where confined clusters of k flipped spins and a given domain wall length become degenerate with the initial state. The single spin flip resonance is at an energy of $h_z^S = -4J$, and at higher energies resonances of larger cluster sizes k follow (see Fig. 1a). The energetic position of the higher-lying collective resonances is

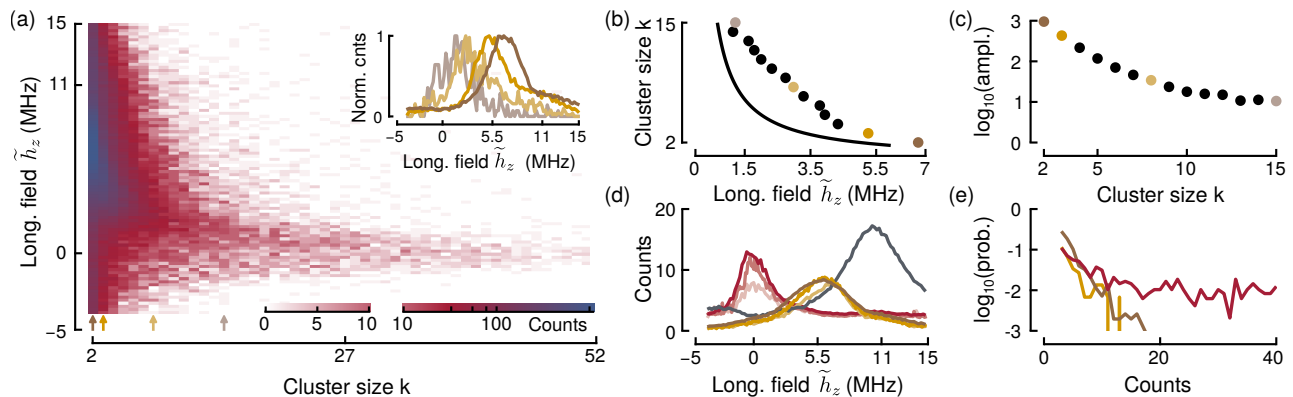


FIG. 2. **Spectral response.** (a) Two-dimensional histogram of the cluster size distribution versus longitudinal field after $2\mu\text{s}$ evolution time with $\Omega_{\text{max}} = 2\pi \times 2.24\text{ MHz}$. To highlight the tails of the distribution, we use a linear color scale up to 10 counts and a logarithmic scale above. The inset shows normalized cuts along the vertical axis for 2-, 3-, 8-, and 15-atom clusters as indicated by the colored arrows. (b) Resonance positions extracted from Gaussian fits to the data shown in the inset of (a) versus cluster size (dots) together with the classical expectation (solid line). The colored dots correspond to the cuts shown in (a). (c) Amplitude of the Gaussian fits versus cluster size. The coloring is as in (b). (d) Mean number of individual flipped spins (gray) and mean number of clusters (brownish colors) together with the mean cluster size (reddish colors) versus longitudinal field. The lighter colors for the cluster number and size indicate data taken at shorter evolution times of $0.5\mu\text{s}$ (light) and $1\mu\text{s}$ (medium-light). (e) Normalized cluster size distribution at the facilitation resonance (red) and at $\tilde{h}_z = \pm 4\text{ MHz}$ (brown, yellow) after $2\mu\text{s}$ evolution time.

determined by the equality of the surface energy cost (J per unsatisfied bond) to the volume energy gain (h_z per flipped spin), resulting in $h_z^C(k) = -2J(k+1)/k$. This series of many-body resonances is constrained to feature no loops in the confined cluster shapes. The energetic cascade of k -sized clusters is bounded from above by a special resonance at $h_z^A = -2J$. At this deconfinement point, all clusters featuring a single loop are resonant, independent of their size. Additionally, clusters with a certain number of kinks (see Fig. 1b, lower-left) are in or near resonance due to the contribution of diagonal interactions, which increase the energy of such clusters. A finite transverse field Ω induces quantum fluctuations leading to a broadening of the resonances and, already for moderate amplitudes, to a non-perturbative renormalization of the confined cluster energies $h_z^C(k)$ [36].

In a first set of experiments, we aim to explore this collective spectral response. We start in the fully polarized $|\downarrow\rangle^{\otimes N}$ state. For different h_z , we abruptly quench the transversal coupling from zero to Ω_{max} and take snapshots of the system after an evolution time of $2\mu\text{s}$. Spin-flipped atoms, that is, atoms excited to the Rydberg state, are lost from the traps due to the anti-trapping nature of the Rydberg state in our optical tweezers. We reconstruct the spin configuration in the \hat{Z} -basis by comparing the tweezer population before and after the quench. Fig. 1c shows a typical final image where we highlight connected clusters of Rydberg atoms. By repeating the experiment for different h_z , we obtain statistics of the cluster size distribution. In the following, we measure the longitudinal field $\tilde{h}_z = -(h_z - h_z^A)$ inverted

and relative to the deconfinement resonance. The resulting two-dimensional histogram is shown in Fig. 2a, where we include only clusters, defined as two or more adjacent spin flips. No feature is visible at the single spin flip resonance $\tilde{h}_z = \tilde{h}_z^S = 11\text{ MHz}$. For decreasing \tilde{h}_z , the cluster size distribution develops a pronounced tail towards large clusters. Vertical cuts at different cluster sizes (inset of Fig. 2a) reveal a series of resonances, which show the expected trend of a smaller \tilde{h}_z for larger cluster size. In Fig. 2b we summarize the resonance positions extracted from Gaussian fits to the cuts together with the classical expectation $\tilde{h}_z^C(k) = 2J/k$. Our analysis reveals collective resonances up to confined cluster sizes of about $k = 15$. We observe a sizeable shift of the resonances towards larger \tilde{h}_z , which we attribute to the quantum fluctuations induced by the strong transverse field Ω . The unresolved diagonal and longer-ranged interactions tend to shift the collective cluster resonances towards smaller \tilde{h}_z .

As we discuss in the supplement [36], the perturbative consideration of the transverse field qualitatively explains the trend of the observed shift but quantitatively fails to reproduce the experimental findings. This underlines the non-perturbative nature of the confined cluster resonances in Ω , an aspect that is also reflected in the scaling of the amplitudes of the resonances as plotted in Fig. 2c. These show a trend towards saturation for larger clusters. Fig. 2d highlights the existence of three qualitatively different regimes in the spectrum. The number of individual flipped spins peaks around the single spin-flip resonance, while smaller clusters dominate the response

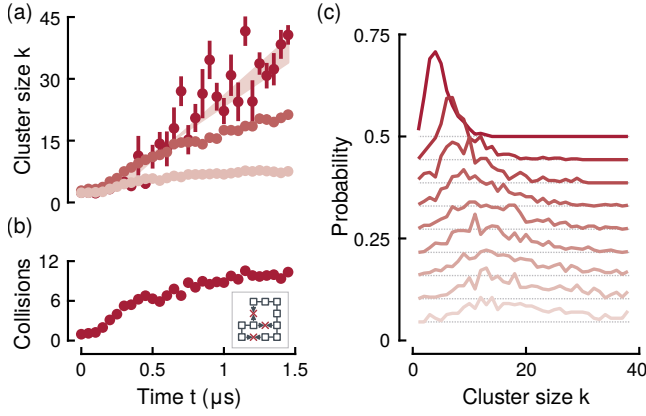


FIG. 3. **Deconfined cluster formation kinetics.** All data is taken on the deconfinement resonance at $\tilde{h}_z = \tilde{h}_z^A = 0$ and with $\Omega_{\text{max}} = 2\pi \times 2.0 \text{ MHz}$. **(a)** Growth dynamics for the two largest clusters in the system. For each run, we identify the two largest clusters and average their sizes individually over all runs (middle red for the largest, light red for the second-largest cluster). In dark red, we show the mean size of the largest cluster conditioned to runs in which only one cluster was identified. A linear fit reveals a growth rate of $24(4) \text{ sites}/\mu\text{s}$, where the uncertainty is dominated by the selection of data points included in the fit (all vs. $t > 0.25 \mu\text{s}$). Error bars indicate the standard error of the mean. **(b)** Number of cluster collisions versus time. A collision is defined as a bond on which cluster growth is blocked by a nearby cluster, that is, where we identify two adjacent \uparrow -spins around a \downarrow -spin and where both \uparrow -spins belong to distinct clusters (see inset). **(c)** Histograms showing the evolution of the distribution of cluster sizes. We bin the data in intervals of $0.15 \mu\text{s}$ and show the area-normalized counts for increasing evolution times from $0.1 \mu\text{s}$ to $1.45 \mu\text{s}$ (dark to light). The individual histograms are offset vertically for better visibility, as indicated by the thin gray lines.

for intermediate \tilde{h}_z . Finally, on the deconfinement resonance, the size of the clusters peaks, and the number of clusters is minimal. The data also shows that the system requires longer times to reach a steady state on the deconfinement resonance and in the regime where large clusters form. The cluster size distribution changes qualitatively on the deconfinement point. While it is strongly peaked in the confined regime, it becomes broad on resonance (see Fig. 2e).

We now turn our focus to the study of the kinetics of the formation of unconfined clusters. To increase the probability of observing cluster growth, we coherently increase the Rydberg population initially before quenching to the deconfinement resonance. To this end, we pulse the Rydberg laser resonantly for a short time to prepare about 4 % of the atoms delocalized in the Rydberg state. While the Rabi driving is off for 200 ns, we jump to the deconfinement resonance and switch on the Rabi drive with Ω_{max} . In Fig. 3a we show the mean size of the two largest clusters as a function of time together with the mean size of the cluster conditioned to only one cluster

identified in the run. We observe rapid and approximately linear-in-time growth of the clusters. In the single cluster case, we observe a growth with constant rate $R = 12 \pm 2 \Omega_{\text{max}}$. The growth rate is much faster than the maximum group velocity expected for domain growth in 1D $R_{1D} = 2\Omega_{\text{max}}$, which follows analytically from the motion of free domain walls [4, 39]. We attribute this speed-up to the presence of multiple bonds, over which growth is active simultaneously. If several clusters are present, the growth rate is initially unchanged, but the growth slows down for the largest cluster at later times, when the size of the second largest cluster approximately saturates. We interpret this simultaneous slowdown as a signature of cluster-cluster interactions, which reduce the effective space available for growth. This picture is supported by the data in Fig. 3b, where we show the number of cluster collisions, defined as the number of bonds on which cluster growth is blocked by a nearby cluster. The collisions show qualitatively similar dynamics as the mean largest cluster size, indicating signs of saturation when the cluster growth slows down. Finally, we show the temporal evolution of the distribution of cluster sizes in Fig. 3c. From being initially peaked, the distribution broadens even quicker than its mean value shifts towards larger sizes. The effect of the initially increased Rydberg population is to suppress small clusters, as reflected in the difference of the late time distribution to the steady state histogram obtained without the initial pulse (cf. Fig. 2e).

To shed light on the constraints governing the shape of the deconfined clusters, we analyze the number of loops in the clusters as a function of time in Fig. 4a. The short time dynamics up to about 250 ns is influenced by the finite rise time of our laser pulses [36] and by artifacts due to the definition of clusters as minimally two adjacent empty sites. After this initial phase, the number of loops grows linearly in time with a slow rate. This contrasts the expectation of a constant loop number: closing a loop means to increase the cluster perimeter by less than two unsatisfied bonds; thus, this process is off-resonant. In fact, we find that the number of missing isolated atoms decreases at a similar rate as the loop number increases. Keeping in mind that the perimeter of the clusters grows with time, this indicates that the detected increase of loops is predominantly explained by our finite recapture fidelity (ca. 95 %). The larger cluster perimeter increases the probability that a detection error induces a false loop, such that the true loop number is indeed constant. The same energetic argument that underlies loop number conservation also prevents clusters from joining during the dynamics. In Fig. 4b we show the evolution of the detected mean cluster number, which indeed saturates quickly and then slightly decreases, which we also attribute to our finite detection fidelity.

In conclusion, we have presented experimental studies of confined and deconfined cluster formation after

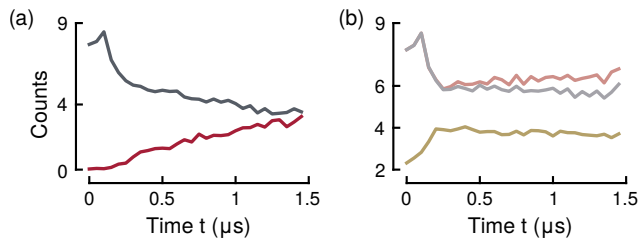


FIG. 4. Shape constraints and cluster number conservation. (a) The number of loops in the clusters versus time (red) and the number of isolated spin flips (gray) show a similar increase (decrease) rate after an initial transient behavior. (b) The light red data shows the sum of the loops and the number of isolated flipped spins. For times larger than $0.25 \mu\text{s}$, this sum is approximately constant. The gray line shows the mean number of isolated spins plus the minimum number of spins in clusters needed to flip down to remove all loops. It saturates fully, as expected for a signal induced by the finite detection fidelity. The mean number of clusters is conserved, as shown by the yellow data that quickly saturates.

quenches in the 2D transverse field Ising model. Our data reveals an intriguing collective response of this paradigmatic quantum many-body system. We observed large confined clusters with resonances, non-perturbatively shifted by quantum fluctuations. On the deconfinement resonance, we observe fast avalanche-like growth of unconfined clusters with strong constraints on the cluster shapes and strong mutual interactions. We presented signatures of a slowdown of the dynamics at later times. Reaching the steady state is hindered by the strong interactions between the extended clusters, effectively constraining each others growth, a characteristic feature of glassy dynamics. Our data on quantum dynamics involving large clusters and strong non-perturbative effects presents a challenge for theoretical modeling and may serve as benchmark data for advanced numerical methods. Experimentally, our work opens several exciting perspectives for future studies of metastability and confinement in 2D lattice systems [7, 33], among them the functional dependence of the confined cluster energies and coupling strengths on the transverse field, false vacuum decay dynamics, or the role of long-range interactions [19]. Changing the 2D array geometry to a Kagome lattice, will allow us to explore lattice gauge theories [40]. Furthermore, our experiments demonstrate coherent facilitated Rydberg dynamics in two-dimensional arrays, opening a new research line with Rydberg arrays and paving the way towards further studies of the physics of Rydberg quantum magnets under facilitation constraints [8–10].

Acknowledgments: We acknowledge discussions with Hannes Pichler, Marco di Liberto, Simone Montangero, Federica Surace and Johannes Zeiher. This work received funding from the Horizon Europe pro-

gram HORIZON-CL4-2022-QUANTUM-02-SGA via the project 101113690 (PASQuanS2.1), the Federal Ministry of Education and Research Germany (BMBF) via the project 13N15974, and the Deutsche Forschungsgemeinschaft within the research units FOR5413 (Grant Nos. 465199066 and 465199066), and through FOR 5522 (Grant No. 499180199) and the SPP 1929 GiRyd (project GR4741/5). We also acknowledge funding through JST-DFG 2024: Japanese-German Joint Call for Proposals on “Quantum Technologies” (Japan-JST-DFG-ASPIRE 2024) under DFG Grant No. 554561799 and from the Alfried Krupp von Bohlen and Halbach Foundation. IL acknowledges support from the European Union through the ERC grant OPEN-2QS (Grant No. 101164443).

Author Contributions: All authors contributed extensively to the planning, data acquisition, or analysis of the results presented here.

Data availability: The experimental and theoretical data and evaluation scripts that support the findings of this study will be available on Zenodo.

Note added: During the preparation of this manuscript, we became aware of a related study in a 1D Rydberg array by the group of Prof. Li You at Tsinghua University Beijing.

SUPPLEMENTAL INFORMATION:

Tweezer array and high fidelity detection

The 225 optical tweezers used in this experiment are generated from a 1064 nm single-mode fiber laser and positioned using a liquid-crystal spatial-light modulator placed in the Fourier plane of our in-vacuum objective. The objective has a numerical aperture (NA) of 0.6 and is covered with a thin gold mesh that isolates the atoms from stray electric fields that may originate from its non-conducting surface.

We detect single ^{39}K atoms in the tweezers by inducing fluorescence on the D2 line while simultaneously cooling the atoms inside the traps in a gray-molasses configuration using the D1 line for 100 ms [41]. To enhance the survival probability to 99 %, we pulse the D2 light with a frequency of 1 kHz. The scattered photons from the D2-light are spectrally separated from the D1-light by four consecutive band-pass filters and imaged onto an EMCCD camera. While the $4S_{1/2}$ ground state has a comparably small polarizability at 1064 nm and experiences negligible vector light shifts, the $4P_{1/2}$ and $4P_{3/2}$ excited states of the D1 and D2 line exhibit light shifts that are more than six times larger, along with sizable vector components. Due to the strong sensitivity of our cooling and imaging scheme to light-shift of the transitions, this makes our imaging a sensitive probe of the tweezers depths. To ensure high-fidelity detection across the entire tweezer array, we homogenize the intensities of the tweezers following the procedure reported in ref. [37]. The local feedback signals for the individual tweezers are extracted from the measured fluorescence strengths of the tweezers. We typically reach a homogeneity of $\approx 1\%$ limited by statistical fluctuations.

Initial state preparation

After an initial MOT loading and compression phase, we cool into our static tweezer array using a gray molasses. To facilitate the loading of the tweezers, we simultaneously apply a strongly elliptical dipole trap with a $7\text{ }\mu\text{m}$ ($130\text{ }\mu\text{m}$) vertical (horizontal) waist. This light-sheet trap enters the vacuum chamber orthogonal to the tweezer beam direction and is aligned to overlap with the focal plane tweezer array. We use 8 W of 1064 nm laser light to form the light sheet. Note that the Rayleigh range is only $\approx 150\text{ }\mu\text{m}$, providing also confinement in the propagation direction. We empirically found that the light-sheet trap helps to stabilize the loading probability of the tweezers against power drifts in the cooling beams. It also increases the confinement along the weaker trapping axis of the tweezer array. The same beam configuration is used during parity-projection by the gray molasses beams, after which only single atoms

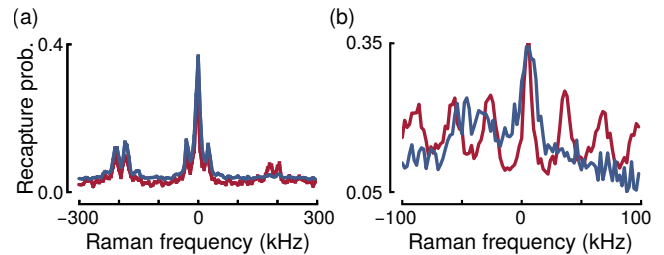


FIG. 5. **Raman sideband cooling.** In red we show the Raman spectra without sideband cooling and in blue with sideband cooling applied. (a) Radial Raman spectrum. (b) Axial Raman spectrum.

remain in the tweezers [42]. We achieve a stable loading of $\approx 65\%$ for a typical loading time of 400 ms.

Subsequently, we take a first picture to determine which optical tweezers were loaded. We then use a crossed acousto-optical deflector (AOD) to reshuffle the atoms for high filling in the central 10×10 tweezers. The AOD tweezer is generated using a 795 nm DBR diode, providing 80 mW. In a single sorting run, we achieve a filling fraction in the central array of 92 %. The same mobile tweezer is used to remove the atoms from all sites neighboring the central 10×10 array.

To prepare the atoms close to the motional ground state of the trap, we apply Raman sideband cooling in the tweezer array and reach a radial (axial) ground-state population of 90 % (85 %). Fig. 5 shows radial and axial Raman spectra with and without Raman sideband cooling. This step is critical to avoid positional disorder that strongly affects the facilitation dynamics. The 1064 nm tweezers induce strong tensor, and for elliptical light also strong vector, light shifts of the $4P$ state manifold. Of particular importance is the $4P_{1/2}$ state used for repumping in the Raman cooling process [35]. The performance of the cooling critically depends on the darkness of the motional ground state, and we found that the state mixing associated with vector light shifts in the excited state quickly deteriorates this darkness. This effect is minimized, by choosing linear polarization of the tweezer light to avoid strong vector light shifts. For the last cycle of the Raman sideband cooling process, we keep the repumping beam on longer to reach a 99 % population in the $4S_{1/2} |F=2, m_F=2\rangle$ state. This sequence initializes the system to near the motional ground state and in the paramagnetic state $|\downarrow\rangle^{\otimes N}$.

Rydberg coupling

We induce the transverse and longitudinal fields by laser-coupling the ground state to selected Rydberg states. From the corresponding dressed-state picture, it becomes evident that the Rabi frequency Ω maps directly

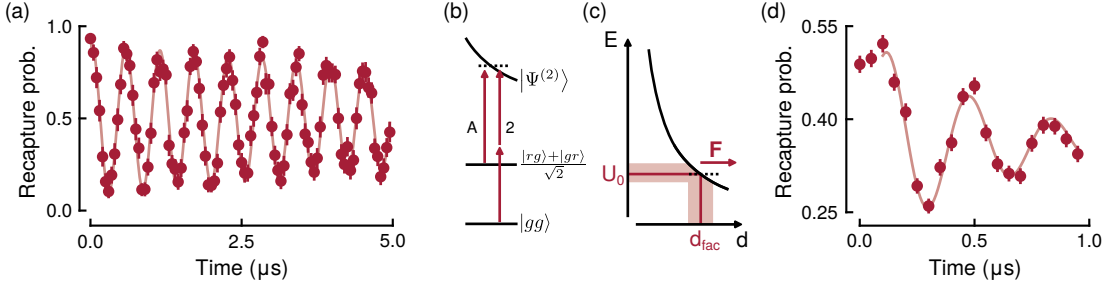


FIG. 6. **Effect of forces on facilitated dynamics of isolated pairs.** (a) Reference data showing Rabi oscillations of a single atom in the array. To avoid interactions, the Rydberg state was changed to 45S. Error bars represent one standard deviation of the mean. We find a $1/e$ -coherence time of 13 μ s at a Rabi frequency of $\Omega = 2\pi \times 1.8$ MHz. (b) Illustration of the facilitation condition, for which the intermediate state with one atom in the Rydberg state is resonantly coupled to the interaction-shifted pair-Rydberg state $|\Psi^{(2)}\rangle$ (marked by "A"). The direct second-order coupling (marked by "2") from the pair-ground $|gg\rangle$ to the pair-Rydberg state is also illustrated. While the facilitation resonance is shifted to U_0 , the second-order transition for isolated pairs is found at $U_0/2$. (c) Illustration of the coupling between spin and motion in facilitation experiments. Positional uncertainty around the facilitation distance d_{fac} , indicated by the light red area, translates to uncertainty in the interaction strength around U_0 . The gradient of the van der Waals force results in a strong repulsive force F . (d) Coherent oscillations for pairs, initialized in the state $\frac{|rg\rangle+|gr\rangle}{\sqrt{2}}$ and then driven on facilitation resonance. Shown is the recapture probability versus coupling time. A small recapture probability corresponds to a large probability for the atom to be in the Rydberg state. We find an symmetry-enhanced oscillation frequency of $\Omega_{pair} = 2\pi \times 2.8$ MHz $\approx 2\pi \times \sqrt{2} \times 2$ MHz and a $1/e$ -decay time of 0.54 μ s.

to the transverse field and the detuning Δ to the longitudinal via $h_z = (\Delta + \frac{\mathcal{N}U_0}{2})$, with U_0 being the interaction shift obtained from the pair interaction potential of two Rydberg atoms and with \mathcal{N} the number of nearest neighbors. The transverse field is implemented by two-photon laser coupling to the Rydberg state. Our ladder scheme connects the $4S_{1/2} |F=2, m_F=2\rangle$ near-resonantly, with a detuning of ≈ 500 MHz to the intermediate state $5P_{3/2} |F=3, m_F=3\rangle$, and then to the $75S |J=1/2, m_J=1/2\rangle$ Rydberg state, while applying 5 G offset field along the beams propagation axis.

The transition from $4S_{1/2} |F=2, m_F=2\rangle$ to $5P_{3/2} |F=3, m_F=3\rangle$ is driven with a titanium-sapphire laser which is doubled to 405 nm, and ≈ 50 mW is guided to the atoms. To couple from the $5P_{3/2} |F=3, m_F=3\rangle$ to the $75S |J=1/2, m_J=1/2\rangle$ state, we use another titanium-sapphire laser at 974 nm, from which ≈ 180 mW reach the atoms. Both lasers are stabilized to resonators made from ultralow-expansion ceramics using Pound-Drever-Hall schemes and feature state-of-the-art phase-noise performance with spectra similar to those measured in refs. [43, 44]. Both beams pass acousto-optical modulators for precise control over the pulses reaching the atoms. To enhance reproducibility of pulse amplitudes, we actively stabilize the laser intensities using photodiodes in a sample-and-hold fashion.

In the experiments described in the main text fast switching of the Rydberg coupling is important. This is achieved by switching on the coupling from $5P_{3/2} |F=3, m_F=3\rangle$ to the $75S |J=1/2, m_J=1/2\rangle$ state shortly before the coupling from $4S_{1/2} |F=2, m_F=2\rangle$ to $5P_{3/2} |F=3, m_F=3\rangle$ state. The switching time is therefore limited by the double pass AOM in the 405 nm

beam path, which is ≈ 200 ns. The effective detuning to the Rydberg state is also controlled by varying the AOM frequency in the 405 nm beam path, while the frequency applied to the AOM in the 974 nm is kept constant.

We shape both of the laser beams for Rydberg coupling into elliptical beams similar to the light sheet. The beams are counter-propagating to each other with the 974 nm beam aligned along the light-sheet axis. Both beams are circularly polarized to maximize the coupling strength to the selected Rydberg state. For the 405 nm beam we measured a vertical (horizontal) waist of 35 μ m (300 μ m) and for the 974 nm beam 10 μ m (170 μ m). Across the array we measure a root-mean-square variation of 7 % of the Rabi frequency. This is dominated by the finite extent of the 974 nm beam in the horizontal direction as well as the vertical Rayleigh range of similar scale. The variation in Rabi frequency manifests in a large scale harmonic envelope over the atom array. The small vertical waists of both beams are required to achieve a high Rabi frequency over the entire array, but make the configuration susceptible to small mechanical fluctuations in the experimental setup. While this effect is reduced for atoms which are at the maximum of the gaussian beams, it is more important for atoms away from the beam center. We observe this effect as a position dependence of the coherence time in our Rabi oscillations. This is our main decoherence effect, which, however, has minimal effect on the timescale of 2 μ s explored in the experiments presented here. The Rabi oscillations to the $45S_{1/2}$ state shown in Fig. 6a underline the excellent coherence of single-atom control achieved in our setup.

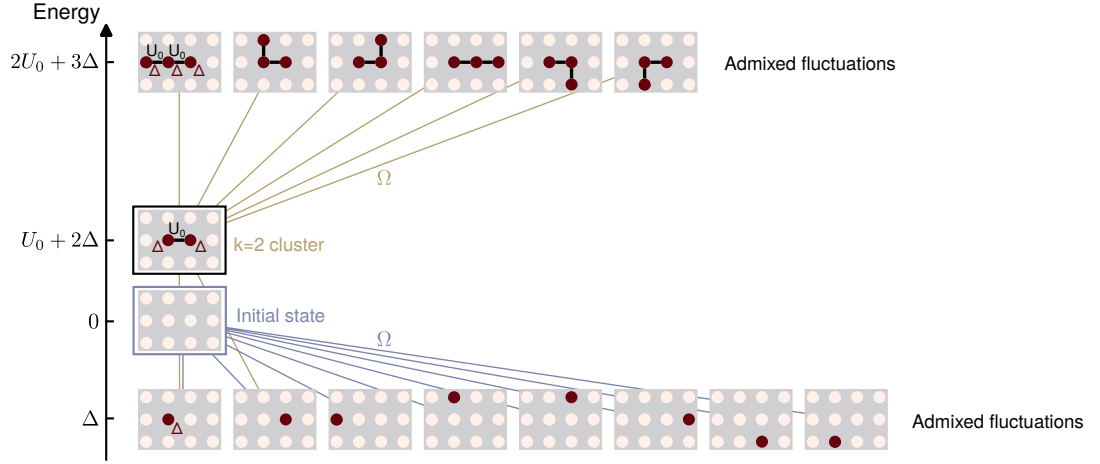


FIG. 7. **Illustration of the contributing terms in 2nd order perturbation theory for the resonance position of confined clusters.** We illustrate the relevant states directly coupled with strength Ω to the $k = 2$ cluster at energy $U_0 + 2\Delta$ and the initial state at energy 0. Relevant are all states, of which the contribution to the calculation of the energy difference of the $k = 2$ cluster and the initial state does not vanish in second order perturbation theory. Top row: Admixed $k = 3$ cluster states at energy $2U_0 + 3\Delta$. Bottom row: Admixed states with an isolated atom in the Rydberg state at energy Δ .

Force

The main experimental challenge is the strong spin-motion coupling on the facilitation resonance [24, 25, 45]. The van der Waals interaction naturally features a strong gradient of $\partial V/\partial d = -6V/d \approx 10 \text{ kHz nm}^{-1}$ (cf. Fig. 6). This has two consequences. First, it translates thermal position disorder into interaction disorder, which hindered early experiments to observe facilitation dynamics [23] and requires near-ground-state initial state preparation. Second, the associated forces are large resulting in an acceleration the order of $10^4 g$ for our parameters, with g the earths gravitational acceleration. An isolated Rydberg pair features the worst case acceleration per atom, which displaces it by about $50 \text{ nm } \mu\text{s}^{-1}$ and thus quickly out of the bandwidth of our transverse field given by $\Omega = 2\pi \times 2 \text{ MHz}$. In Fig. 6d we show that we indeed observe coherent oscillations of Rydberg pairs on the facilitation resonance for more than $1 \mu\text{s}$. For this measurement, we prepared isolated pairs of $7 \mu\text{m}$ distance and initialized them with one atom in the Rydberg state by a π -pulse under Rydberg blockade conditions. After the pulse we quickly jumped the laser frequency to facilitation resonance. To remain approximately in the coherent regime, we limited all our studies presented here to similarly short times, even though, clusters are likely less impacted by the motion due to balancing forces [45].

Breakdown of perturbation theory for the resonance position of confined clusters

In the following we outline the perturbative calculation for determining the resonance position of the Ry-

dberg clusters, using as example the case $k = 2$. In the absence of the coupling laser the state $|\downarrow\rangle^{\otimes N}$ is an eigenstate of the many-body Hamiltonian with energy $E_0^{(0)}$. Furthermore, a $k = 2$ cluster has the eigenenergy $E_1^{(0)} = \Delta + 2U_0$. The energy difference of the two states is thus $E_1^{(0)} - E_0^{(0)} = \Delta + 2U_0$. As shown in Fig. 7 both states are dressed by energetically nearby states, once the Rydberg excitation laser with Rabi frequency Ω is applied. Applying second order perturbation theory in Ω/Δ then yields the renormalized energy difference

$$\begin{aligned} E_1 - E_0 &= \left(E_1^{(0)} - E_0^{(0)}\right) + \left(E_1^{(2)} - E_0^{(2)}\right) \\ &= \Delta + 2U_0 + \frac{\Omega^2}{4} \left[\frac{6}{(2\Delta + U_0) - (3\Delta + 2U_0)} \right. \\ &\quad \left. + \frac{2}{(2\Delta + U_0) - \Delta} - \frac{8}{0 - \Delta} \right] \\ &= \Delta + 2U_0 + \frac{\Omega^2}{4} \left[-\frac{4}{\Delta + U_0} + \frac{8}{U_0} \right]. \end{aligned} \quad (1)$$

From this expression it becomes evident, that choosing $\Delta = -\frac{U_0}{2}$ no longer leads to a resonant two-photon excitation of the $k = 2$ cluster from the state $|\downarrow\rangle^{\otimes N}$. Instead one needs to choose a slightly shifted detuning, which for $|\Delta| \gg U_0$ is given by

$$\Delta^{(2)} \approx -\frac{U_0}{2} + 3\frac{\Omega^2}{U_0}. \quad (2)$$

As can be seen in Fig. 2(b) of the main text, such shift of the resonance position is observed systematically for all cluster sizes. However, in the experiment we use a comparably large ratio $|\Omega/\Delta| \approx 2\Omega/U_0 \approx 2/5$, at which higher order terms become important. In fact, the sec-

ond order equation Eq. (1) does not yield a physical solution anymore. Quantum fluctuations strongly affect the confined cluster energies due to the many contributing configurations in an extended 2D lattice.

* christian.gross@uni-tuebingen.de

- [1] S. B. Rutkevich, Decay of the metastable phase in $d=1$ and $d=2$ Ising models, *Phys. Rev. B* **60**, 14525 (1999).
- [2] G. Lagnese, F. M. Surace, M. Kormos, and P. Calabrese, False vacuum decay in quantum spin chains, *Phys. Rev. B* **104**, L201106 (2021).
- [3] C. Yin, F. M. Surace, and A. Lucas, Theory of Metastable States in Many-Body Quantum Systems, *Phys. Rev. X* **15**, 011064 (2025).
- [4] M. Kormos, M. Collura, G. Takács, and P. Calabrese, Real-time confinement following a quantum quench to a non-integrable model, *Nature Phys* **13**, 246 (2017).
- [5] D. Gribben, I. Lesanovsky, and R. Gutiérrez, Quench dynamics of a dissipative Rydberg gas in the classical and quantum regimes, *Phys. Rev. A* **97**, 011603 (2018).
- [6] F. Liu, R. Lundgren, P. Titum, G. Pagano, J. Zhang, C. Monroe, and A. V. Gorshkov, Confined Quasiparticle Dynamics in Long-Range Interacting Quantum Spin Chains, *Phys. Rev. Lett.* **122**, 150601 (2019).
- [7] L. Pavešić, D. Jaschke, and S. Montangero, Constrained dynamics and confinement in the two-dimensional quantum Ising model, *Phys. Rev. B* **111**, L140305 (2025).
- [8] B. Everest, M. Marcuzzi, J. P. Garrahan, and I. Lesanovsky, Emergent kinetic constraints, ergodicity breaking, and cooperative dynamics in noisy quantum systems, *Phys. Rev. E* **94**, 052108 (2016).
- [9] F. Balducci, A. Gambassi, A. Leroise, A. Scardicchio, and C. Vanoni, Localization and Melting of Interfaces in the Two-Dimensional Quantum Ising Model, *Phys. Rev. Lett.* **129**, 120601 (2022).
- [10] O. Hart and R. Nandkishore, Hilbert space shattering and dynamical freezing in the quantum Ising model, *Phys. Rev. B* **106**, 214426 (2022).
- [11] W. L. Tan, P. Becker, F. Liu, G. Pagano, K. S. Collins, A. De, L. Feng, H. B. Kaplan, A. Kyprianidis, R. Lundgren, W. Morong, S. Whitsitt, A. V. Gorshkov, and C. Monroe, Domain-wall confinement and dynamics in a quantum simulator, *Nat. Phys.* **17**, 742 (2021).
- [12] Z.-H. Zhu, Y. Liu, G. Lagnese, F. M. Surace, W.-Y. Zhang, M.-G. He, J. C. Halimeh, M. Dalmonte, S. C. Morampudi, F. Wilczek, Z.-S. Yuan, and J.-W. Pan, Probing false vacuum decay on a cold-atom gauge-theory quantum simulator (2024), arXiv:2411.12565.
- [13] D. Luo, F. M. Surace, A. De, A. Leroise, E. R. Bennewitz, B. Ware, A. Schuckert, Z. Davoudi, A. V. Gorshkov, O. Katz, and C. Monroe, Quantum simulation of bubble nucleation across a quantum phase transition (2025), arXiv:2505.09607.
- [14] J. Vodeb, J.-Y. Desaulles, A. Hallam, A. Rava, G. Humar, D. Willsch, F. Jin, M. Willsch, K. Michielsen, and Z. Papić, Stirring the false vacuum via interacting quantized bubbles on a 5,564-qubit quantum annealer, *Nat. Phys.* **21**, 386 (2025).
- [15] A. Zenesini, A. Berti, R. Cominotti, C. Rogora, I. G. Moss, T. P. Billam, I. Carusotto, G. Lamporesi, A. Re-
cati, and G. Ferrari, False vacuum decay via bubble formation in ferromagnetic superfluids, *Nat. Phys.* **20**, 558 (2024).
- [16] D. González-Cuadra, M. Hamdan, T. V. Zache, B. Braverman, M. Kornjača, A. Lukin, S. H. Cantú, F. Liu, S.-T. Wang, A. Keesling, M. D. Lukin, P. Zoller, and A. Bylinskii, Observation of string breaking on a $(2 + 1)$ D Rydberg quantum simulator, *Nature* **642**, 321 (2025).
- [17] L. Hruby, N. Dogra, M. Landini, T. Donner, and T. Esslinger, Metastability and avalanche dynamics in strongly correlated gases with long-range interactions, *Proc. Natl. Acad. Sci.* **115**, 3279 (2018).
- [18] B. Song, S. Dutta, S. Bhawe, J.-C. Yu, E. Carter, N. Cooper, and U. Schneider, Realizing discontinuous quantum phase transitions in a strongly correlated driven optical lattice, *Nat. Phys.* **18**, 259 (2022).
- [19] T. Kaltenmark, C. Nill, C. Groß, and I. Lesanovsky, Spectroscopic signatures of emergent elementary excitations in a kinetically constrained long-range interacting two-dimensional spin system (2025), arXiv:2511.13279.
- [20] A. Browaeys and T. Lahaye, Many-body physics with individually controlled Rydberg atoms, *Nat. Phys.* **16**, 132 (2020).
- [21] C. Ates, T. Pohl, T. Pattard, and J. M. Rost, Antiblockade in Rydberg Excitation of an Ultracold Lattice Gas, *Phys. Rev. Lett.* **98**, 023002 (2007).
- [22] W. Li, C. Ates, and I. Lesanovsky, Nonadiabatic motional effects and dissipative blockade for rydberg atoms excited from optical lattices or microtraps, *Phys. Rev. Lett.* **110**, 213005 (2013).
- [23] M. Marcuzzi, J. Minář, D. Barredo, S. de Léséleuc, H. Labuhn, T. Lahaye, A. Browaeys, E. Levi, and I. Lesanovsky, Facilitation dynamics and localization phenomena in rydberg lattice gases with position disorder, *Phys. Rev. Lett.* **118**, 063606 (2017).
- [24] T. Schlegel, E. Konstantinidou, M. Fleischhauer, and D. Brady, Dephasing in Rydberg Facilitation Due to State-Dependent Dipole Forces (2025), arXiv:2505.09314.
- [25] L. Zhao, P. R. Datla, W. Tian, M. M. Aliyu, and H. Loh, Observation of quantum thermalization restricted to Hilbert space fragments, *Phys. Rev. X* **15**, 011035 (2025).
- [26] P. R. Datla, L. Zhao, W. W. Ho, N. Klco, and H. Loh, Statistical Localization in a Rydberg Simulator of $U(1)$ Lattice Gauge Theory (2025), arXiv:2505.18143.
- [27] H. Schempp, G. Günter, M. Robert-de-Saint-Vincent, C. S. Hofmann, D. Breyel, A. Komnik, D. W. Schönleber, M. Gärttner, J. Evers, S. Whitlock, and M. Weidemüller, Full counting statistics of laser excited rydberg aggregates in a one-dimensional geometry, *Phys. Rev. Lett.* **112**, 013002 (2014).
- [28] N. Malossi, M. M. Valado, S. Scotto, P. Huillery, P. Pillet, D. Ciampini, E. Arimondo, and O. Morsch, Full counting statistics and phase diagram of a dissipative rydberg gas, *Phys. Rev. Lett.* **113**, 023006 (2014).
- [29] A. Urvoy, F. Ripka, I. Lesanovsky, D. Booth, J. P. Shaffer, T. Pfau, and R. Löw, Strongly correlated growth of rydberg aggregates in a vapor cell, *Phys. Rev. Lett.* **114**, 203002 (2015).
- [30] S. Helmrich, A. Arias, G. Lochead, T. M. Wintermantel, M. Buchhold, S. Diehl, and S. Whitlock, Signatures of self-organized criticality in an ultracold atomic gas, *Nature* **577**, 481 (2020).

- [31] D. Brady, J. Bender, P. Mischke, T. Niederprüm, H. Ott, and M. Fleischhauer, Griffiths Phase in a Facilitated Rydberg Gas at Low Temperature (2023), arXiv:2302.14145.
- [32] T. Zhang and Z. Cai, Quantum Slush State in Rydberg Atom Arrays, *Phys. Rev. Lett.* **132**, 206503 (2024).
- [33] L. Pavešić, M. D. Liberto, and S. Montangero, Scattering and induced false vacuum decay in the two-dimensional quantum Ising model (2025), arXiv:2509.02702.
- [34] N. Pancotti, G. Giudice, J. I. Cirac, J. P. Garrahan, and M. C. Bañuls, Quantum East Model: Localization, Non-thermal Eigenstates, and Slow Dynamics, *Phys. Rev. X* **10**, 021051 (2020).
- [35] N. Lorenz, L. Festa, L.-M. Steinert, and C. Gross, Raman sideband cooling in optical tweezer arrays for Rydberg dressing, *SciPost Phys.* **10**, 052 (2021).
- [36] See supplemental material.
- [37] Y. T. Chew, M. Poitrinal, T. Tomita, S. Kitade, J. Mauricio, K. Ohmori, and S. de Léséleuc, Ultraprecise holographic optical tweezer array, *Phys. Rev. A* **110**, 053518 (2024).
- [38] S. Darbha, M. Kornjača, F. Liu, J. Balewski, M. R. Hirsbrunner, P. L. S. Lopes, S.-T. Wang, R. Van Beeumen, D. Camps, and K. Klymko, False vacuum decay and nucleation dynamics in neutral atom systems, *Phys. Rev. B* **110**, 155103 (2024).
- [39] H. C. Fogedby, The Ising chain in a skew magnetic field, *J. Phys. C: Solid State Phys.* **11**, 2801 (1978).
- [40] L. Homeier, A. Pizzi, H. Zhao, J. C. Halimeh, F. Grusdt, and A. M. Rey, Prethermal gauge structure and surface growth in Z2 lattice gauge theories (2025), arXiv:2510.12800.
- [41] J. Ang'ong'a, C. Huang, J. P. Covey, and B. Gadway, Gray molasses cooling of ^{39}K atoms in optical tweezers, *Phys. Rev. Res.* **4**, 013240 (2022).
- [42] B. J. Lester, N. Luick, A. M. Kaufman, C. M. Reynolds, and C. A. Regal, Rapid production of uniformly filled arrays of neutral atoms, *Phys. Rev. Lett.* **115**, 073003 (2015).
- [43] X. Jiang, J. Scott, M. Friesen, and M. Saffman, Sensitivity of quantum gate fidelity to laser phase and intensity noise, *Phys. Rev. A* **107**, 042611 (2023).
- [44] T. Denecker, Y. T. Chew, O. Guillemant, G. Watanabe, T. Tomita, K. Ohmori, and S. de Léséleuc, Measurement and feedforward correction of the fast phase noise of lasers, *Phys. Rev. A* **111**, 042614 (2025).
- [45] G. Emperauger, M. Qiao, G. Bornet, Y. T. Chew, R. Martin, B. Gély, L. Klein, D. Barredo, T. Lahaye, and A. Browaeys, Probing spin-motion coupling of two Rydberg atoms by a Stern-Gerlach-like experiment (2025), arXiv:2508.08899.